AGU100 ADVANCING EARTH AND SPACE SCIENCE

Geophysical Research Letters

RESEARCH LETTER
10.1029/2018GL078297

Key Points:
- Our InSAR-based estimate of the source parameters indicates a deep event with two probable families of models
- We detect a precursory phase using template matching at teleseismic distances to the mainshock
- A transient pulse of fluids is required to trigger this event, maybe a common stress perturbation at the origin of intraplate events

Supporting Information:
- Supporting Information S1

Correspondence to:
R. Jolivet and B. Gardonio,
romain.jolivet@ens.fr;
gardonio@geologie.ens.fr

Citation:
Gardonio, B., Jolivet, R., Calais, E., & Leclère, H. (2018). The April 2017 M_w6.5 Botswana earthquake: An intraplate event triggered by deep fluids. *Geophysical Research Letters*, *45*, 8886–8896. https://doi.org/10.1029/2018GL078297

Received 10 APR 2018
Accepted 9 JUL 2018
Accepted article online 13 JUL 2018
Published online 2 SEP 2018

The April 2017 M_w6.5 Botswana Earthquake: An Intraplate Event Triggered by Deep Fluids

B. Gardonio[1], R. Jolivet[1], E. Calais[1], and H. Leclère[1]

[1]Laboratoire de Géologie, Département de Géosciences, École Normale Supérieure, CNRS UMR 8538, PSL Research University, Paris, France

Abstract Large earthquakes in stable continental regions remain puzzling as; unlike at plate boundaries, they do not result from the local buildup of strain driven by plate tectonics. The 2017 M_w6.5, Bostwana normal faulting earthquake occurred in a region devoid from recent tectonic activity and where present-day deformation is negligible. The depth of the event (29 ± 4 km), in a felsic lower crust where ductile deformation is expected, likely requires a transient pulse of fluids from a deep source to activate brittle faulting. The mainshock was preceded by two foreshock swarm-like sequences that may be further evidence for fluid movement in a critically loaded fault network. Contrary to plate boundary events, the M_w6.5 Botswana earthquake did not require prior localized stress or strain accumulation. We propose that the crust in stable continental regions, even long after the last tectonic episode, constitutes a reservoir of elastic stress that can be released episodically, for instance, as a result of deep fluid migration.

Plain Language Summary Most earthquakes occur at plate boundaries where stress and strain concentrate due to the continuous motion imposed by plate tectonics. However, a significant number of large earthquakes also occur within continents, far from any deforming area. How they are triggered and what is the source of the released stress in such a context are key questions that remain unresolved. We use geodetic data to show that the April 2017 Botswana earthquake, the largest intraplate earthquake in the last 30 years, occurred at a depth of 30 km where rocks flow and should not break. We explore potential mechanisms to explain rock failure at such depth and propose that a local pulse of fluid was responsible for a transient embrittlement of the lower crust. This example shows that, even long after previous mountain building episodes, the crust in stable continental regions remains a reservoir of stress that can be tapped in by earthquakes triggered by local perturbations, including pulses of deep fluids.

1. Introduction

While earthquakes primarily occur along plate boundaries, where most of the tectonic strain is released, large events also strike stable continental interiors, although much less frequently (e.g., Calais et al., 2016; Johnston, 1989). The New Madrid region of the Central United States, with four $M>7$ events between December 1811 and February 1812, is a type locale for large earthquakes in such settings (e.g., Hough et al., 2000; Johnston, 1996; Nuttli, 1973), and examples can be found in all continents. South Africa was struck in 1969 by the M_w6.3 Ceres earthquake (Kruger & Scherbaum, 2014), and in 1998, the Tennant Creek sequence of M_s 6.3, 6.4, and 6.7 events shook central Australia (Bowman, 1992). Careful studies of such rare events are important as the mechanism leading to stress release on faults in regions of very low tectonic deformation remains poorly understood, leading to large uncertainties in hazard assessment in populated continental interiors (e.g., Allman & Smolka, 2001; Liu & Stein, 2016). We focus on the largest stable continental interior earthquake since the 1998 Tennant Creek events, a M_w 6.5 normal faulting earthquake that ruptured a blind fault in Botswana on 3 April 2017, within the Kalahari cratonic domain, far from any identified active fault (Figure 1).

The M_w6.5 Bostwana earthquake occurred close to the junction between the Archean Kaapval craton and the Paleoproterozoic Mahalapye granite of the Limpopo belt (Figure 1). It may have reactivated one of the high angle faults that mark the boundary between these old and seismically quiet geological units (Kolawole et al., 2017). Seismic activity in its epicentral region (−25°S to −21°S, 23°E to 27°E) is more elevated than typical stable continental interiors, with 23 earthquakes of magnitude larger than 4 detected since 1

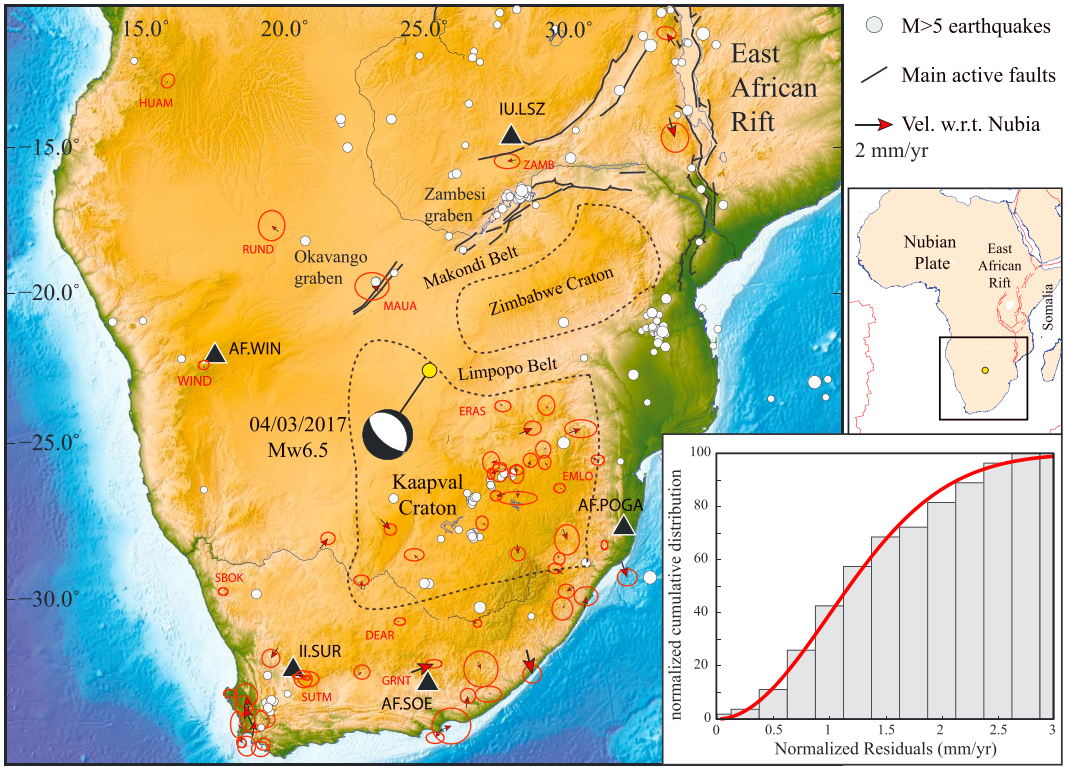

Figure 1. Regional context. Map of the southern tip of the African continent. The NEIC epicenter of the 3 April 2017 Bostwana earthquake is shown with a yellow circle, with its global centroid moment tensor focal mechanism. Black triangles indicate the location of seismological stations used for template matching. Gray dots are earthquake epicenters from the NEIC catalog covering the 1974–2018 time interval. Dotted lines show the boundaries of the Kaapval and Zimbabwe archean cratons. Solid black lines show major faults associated with recent topographic features. Red arrows show residual GPS velocities with respect to a rigid plate assumption with their 95% confidence ellipse. Uncertainties include site-dependent, time-correlated colored noise. Red labels indicate the code name of some of the GPS stations. Lower right inset shows the normalized cumulative distribution of GPS velocity residuals (both north and east components). The red line shows the theoretical χ^2 distribution expected if residuals are normally distributed in two dimensions with a unit variance. NEIC = National Earthquake Information Center; GPS = Global Positioning System.

January 2000. The mainshock was followed by about 30 aftershocks of magnitude greater than 3, as reported by the International Seismological Center (ISC). Aftershocks appear to first extend over a large region before focusing closer to the epicenter, though this may be biased by the location capability of small events at teleseismic distances. One of the objectives of this study is to expand this aftershock catalog and, more importantly, to search for potential foreshocks, using for the first time a template matching technique at teleseismic distances from the mainshock.

Although southern Africa experiences diffuse, low-magnitude seismicity (e.g., Pastier et al., 2017), no active structure has been identified in the epicentral region of the Botswana earthquake. The nearest active faults are 350 km to the north bounding the isolated Okavango tectonic basin, where a M6.7 earthquake occurred in 1952 (Modisi et al., 2000; Reeves, 1972). This basin has been interpreted by some as an incipient rift at the western end of a belt of weak seismicity that extends from the Okavango basin through the Kariba graben to the east and connects to the Rukwa region of the East African Rift (Modisi et al., 2000; Scholz et al., 1976), although that interpretation has recently been challenged (Pastier et al., 2017). The 2017 Bostwana earthquake is located well away from these structures. Its global centroid moment tensor (GCMT) mechanism and fault plane solutions derived from differential interferometric synthetic aperture radar (InSAR) data show a fault plane striking perpendicular to this possible direction of rift propagation (Albano et al., 2017; Kolawole et al., 2017). However, these published InSAR-derived fault models did not explore the whole range of possible fault planes and another objective of this study is to reevaluate the source mechanism and depth of this earthquake.

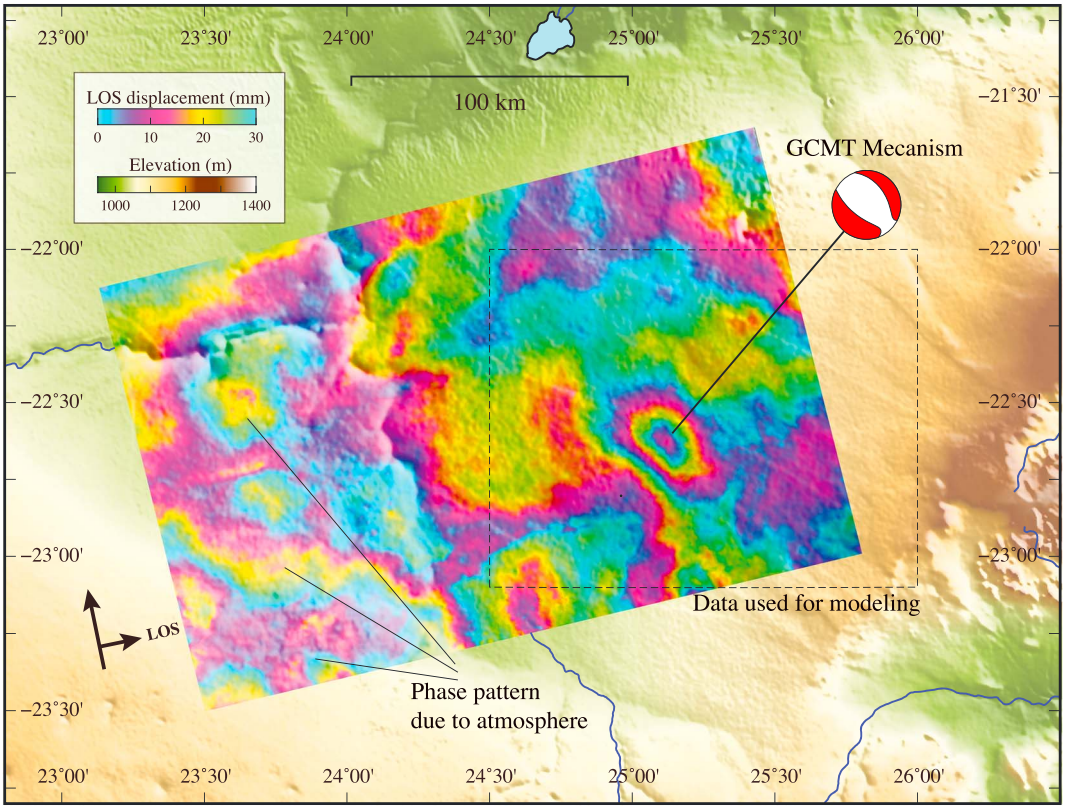

Figure 2. Interferometric synthetic aperture radar data. Interferogram derived from Sentinel 1 acquisitions on 30 March and 11 April 2017. One color fringe indicates 3 cm of displacement in the satellite line of sight (thick black arrow). Dotted line rectangle indicates the subset of data used for the Bayesian modeling. Focal mechanism is from GCMT (Ekström et al., 2012). Background color is the digital elevation model from Shuttle Radar Topography Mission (Farr & Kobrick, 2000). Blue lines indicate major rivers. GCMT = global centroid moment tensor; LOS = line of sight.

In the following, we show that the Bostwana earthquake (1) occurred at a depth of 29 km, in the lower crust, on a 73° or a 17° dipping fault, and (2) was preceded by two foreshock sequences. We argue that this earthquake sequence was triggered by a local and transient pulse of elevated pore fluid pressure in a lower crust where viscous deformation should otherwise prevail.

2. InSAR Analysis and Bayesian Source Parameters Estimation

We compute an interferogram from Sentinel-1 acquisitions in interferometric wide-swath mode on 30 March and 11 April 2017 along ascending orbits (see the supporting information). We identify surface displacements resulting from this normal faulting event as the oval-shaped set of fringes located in the epicentral region (Figure 2). We measure about 4 cm of coseismic surface displacement in the satellite line of sight. Given the incidence angle of the radar signal in the epicentral region and assuming negligible horizontal motion, this corresponds to about 6 cm of subsidence.

We use a Bayesian formulation to invert for the source parameters of the mainshock. The goal is to find whether it is possible to discriminate between the two possible fault planes provided by the GCMT solution. We select a subset of the interferogram and downsample the interferometric phase using a curvature-based quadtree algorithm (Figure 2 and supporting information Figure S1; Simons et al., 2002). Our model setup includes a single fault plane with constant slip embedded in an elastic homogeneous medium. We solve for the fault centroid position (longitude, latitude, and depth), its orientation (strike and dip), and the amount of slip along dip. We consider its size fixed (10 km along dip and 30 km along strike, chosen based on orders of magnitude for M_w 6 earthquakes) as these size parameters trade-off with slip. In addition, we solve for a constant offset to add to the InSAR data.

Following Bayes's theorem, we write the posterior probability density function (PDF) of the model, $P(\mathbf{m}|\mathbf{d})$, as proportional to the product of the prior PDF, $P(\mathbf{m})$, and the likelihood, $P(\mathbf{d}|\mathbf{m})$,such as

$$P(\mathbf{m}|\mathbf{d}) \propto P(\mathbf{m})P(\mathbf{d}|\mathbf{m}), \tag{1}$$

where **m** is the vector of model parameters and **d** the vector of data to invert (i.e., here the downsampled surface displacements from InSAR). We use uniform distributions for the prior PDF, imposing positivity on slip (i.e., the fault has to be a normal fault). We use a Gaussian formulation for the likelihood, $P(\mathbf{d}|\mathbf{m})$, that writes

$$P(\mathbf{d}|\mathbf{m}) \propto e^{-\frac{1}{2}(\mathbf{Gm}-\mathbf{d})^T\mathbf{C}_\mathrm{d}^{-1}(\mathbf{Gm}-\mathbf{d})}, \tag{2}$$

where **G** is the matrix of Green's functions relating source parameters to surface displacements and $\mathbf{C}_\mathrm{d}$ is the data covariance matrix. We build the Green's functions using Okada's formulation of the surface displacements produced by slip on a rectangular dislocation (Okada, 1985). We use the covariance function of the interferogram to build the data covariance matrix, describing the influence of turbulent tropospheric noise (see the supporting information; Jolivet et al., 2015).

In the present case, the posterior PDF must be multimodal as both southwest and northeast dipping fault planes should be able to fit surface displacements. Using a classic sampling approach, for instance, based on the long-used Metropolis algorithm, will unlikely resolve directly the complete shape of the PDF as the probability for one Markov chain to jump between isolated, high probability regions of the model space is very low. This is likely why a previously published Bayesian model does not show multiple modes for the posterior PDF, hence multiple possible dip angles (Albano et al., 2017). Even if this probability is not null and sampling all regions of the model space should theoretically be possible with a classic Metropolis algorithm (Xu et al., 2015), a prohibitive number of steps would be required. Furthermore, it would be difficult to assert the respective importance of each mode. We use instead the AlTar sampler, specifically designed for high-dimensional problems and complex PDF sampling (see the supporting information).

Our posterior PDF shows four family of models, including two equally likely and two equally less likely that we separate using a K-mean clustering algorithm (supporting information Figure S3). The two most likely families of models have an average depth of 29 ± 4 km and an average magnitude of 6.54 ± 0.05, and their centroid location is consistent with that from GCMT. Members from these two families only differ by their dip angle, one being on average 17° ± 4° and the other at 73° ± 4°, hence the two possible families of strike angle at 180° from each other. These values are similar to those of the conjugate planes of the GCMT solution, with slightly steeper or shallower dip angles for the steep—and a shallow—angle planes, respectively. The InSAR-derived centroid location and magnitude are consistent within uncertainties with those determined by GCMT. We will not further consider the less likely families as their fault strike and magnitude, centroid location, and depth are not consistent with the seismologically derived ones. Finally, our results indicate that it is not possible to discriminate between a steep and a shallow angle normal faulting event as both families of models are equiprobable.

3. Aftershocks and Foreshocks Detection

We then seek to detect aftershocks and possible foreshocks of the Botswana earthquake. Since no data from local seismic networks were available at the time of this work, we apply template matching to continuous signals recorded at teleseismic distances (1,200 to 2,000 km) to the mainshock from November 2016 to April 2017. This technique has been used to detect low-frequency earthquakes within tremor signals (Shelly et al., 2007) or to recover missing events in aftershock (Lengliné & Marsan, 2009; Peng & Zhao, 2009) and foreshock sequences (Bouchon et al., 2011; Gardonio, 2017; Kato & Nakagawa, 2014; Kato et al., 2012; Lengliné et al., 2012). It is, however, more challenging at teleseismic distances because of the much lower signal-to-noise ratio of the seismic records compared to near-field observations.

We select as templates 18 M>3 aftershocks that occurred in the week following the main event to compute their coherence with continuous seismic records at five teleseismic stations (Figure 1). We obtain a continuous record of the coherence per template and per day. We define a coherence threshold above, which we consider that an event has been detected (see the supporting information). Figure 3 shows the cumulative number of events detected at least at two teleseismic stations using coherence thresholds of 0.89, 0.9, and 0.91 after removing autodetections, that is, detections of a template by itself. As expected, the number of detections increases with decreasing threshold. All events are seismic in origin, but some of the lower-threshold ones are

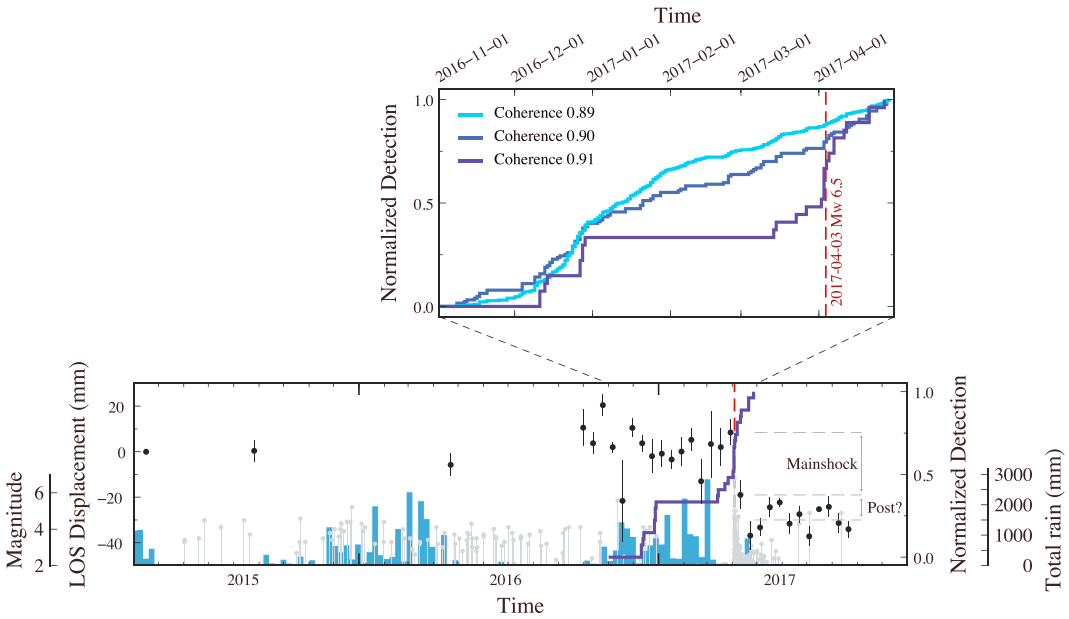

Figure 3. Template matching detection and InSAR time series. (top) Normalized number of template detections as a function of time from November 2016 to late April 2017 for three coherence thresholds. The red dotted line indicates the time of the Botswana M_w 6.5 earthquake. (bottom) Black dots are the differential displacement at the time of Sentinel-1 acquisitions between the epicentral region (average of pixels located less than 10 km away from the maximum displacement) and a stable region (average of pixels located between 50 and 100 km away from the maximum displacement). Blue line is the normalized number of template detections for a coherence threshold of 0.91. Light blue bars are the cumulative rain fall summed over weekly periods. No obvious relationship can be found between hydrological loads besides the fact that the earthquake occurred at the end of the rainfall period. Gray lines and dots are earthquake occurrences and their magnitude from the International Seismological Center catalog. Rainfall and earthquakes are considered between 19° and 30° of longitude and 27° and 17° of latitude south. LOS = line of sight.

located up to 35 km away from the mainshock epicenter, suggesting a fairly broad seismically active region both before and after the mainshock. We also observe, for all detection thresholds, an increase in seismicity between 4 and 30 December 2016—4 months before the main event—while only one M4.1 earthquake was reported by the ISC within 120 km of the mainshock during that same time interval.

At the 0.91 coherence threshold, we detect a total of 20 new events (Table 1). We manually checked these detections for each station. This number is expectedly much smaller than near-field template matching studies (Kato et al., 2012; Kato & Nakagawa, 2014; Lengliné et al., 2012) but nevertheless shows a remarkable temporal distribution, with two sequences of foreshocks. The first one occurs between 4 and 3 months before the mainshock, with nine events detected by templates southwest of the mainshock epicenter (supporting information Figure S4). Its is followed by a seismically quiet time interval until early March. The second foreshock sequence occurs during the 2 weeks that precede the main event, with five events detected by three templates northwest of the mainshock.

4. A Precursory Geodetic Signal?

By reference to other preparatory phases identified before large earthquakes, the foreshocks detected here may be embedded in a broader aseismic event (Bouchon et al., 2011; Ruiz et al., 2014). In order to detect such an event, we processed all available Sentinel-1 acquisitions between April 2015 and August 2017 (supporting information). The resulting time series of relative surface displacements between the epicentral region (<10 km from the epicenter) and the far-field (>60 km from the epicenter) shows no significant signal within the precursory phase during which small earthquakes are detected (Figure 3). The same holds for the full time series (supporting information Figures S8–S11). The coseismic signal is well recovered, with a 2- to 3-cm offset at the time of the mainshock. Averaging over the last 11 acquisitions of the time series suggests that the coseismic offset is followed by up to 1 cm of postseismic displacements.

Table 1
Catalog of the Newly Detected Events

Year	Month	Day	Hour	Minute	Second	Latitude	Longitude	Magnitude
2016	12	11	17	9	32.05	−22.5367	24.9746	3.3
2016	12	11	19	28	14.05	−22.6610	25.0010	3.5
2016	12	13	21	46	46.05	−22.5367	24.9746	3.3
2016	12	14	17	22	52.05	−22.6610	25.0010	3.6
2016	12	27	12	1	44.05	−22.6913	25.1021	3.6
2016	12	27	16	16	18.05	−22.6610	25.0010	3.8
2016	12	28	10	56	54.05	−22.9860	25.1260	3.7
2016	12	28	15	12	22.05	−22.6610	25.0010	3.4
2016	12	29	7	39	24.05	−22.9870	24.9980	3.7
2017	03	14	18	38	20.05	−22.5646	25.0868	3.1
2017	03	15	15	12	2.050	−22.6610	25.0010	3.9
2017	03	23	17	43	12.05	−22.5367	24.9746	3.5
2017	03	27	10	18	4.050	−22.6610	25.0010	3.9
2017	04	02	8	30	40.05	−22.5367	24.9746	3.5
2017	04	05	12	29	10.05	−22.3206	25.4211	3.4
2017	04	11	11	57	32.05	−22.5367	24.9746	3.5
2017	04	12	19	3	28.05	−22.8180	24.9340	3.8
2017	04	21	11	52	4.050	−22.5367	24.9746	3.5
2017	04	21	21	36	48.05	−22.6610	25.0010	3.6
2017	04	27	5	36	56.05	−22.6784	25.1558	3.3

Note. The time of occurrence corresponds to the time at which coherency between the template and the continuous signal is the highest. The locations of the detected events are the same as the location of the template they matched, as indicated in the International Seismological Center catalog. Magnitudes are estimated by calculating the amplitude ratio (see supporting information).

5. Present-Day Regional Strain Accumulation?

The location of the Bostwana earthquake far from areas of concentrated seismic activity, in a region with no morphological evidence of recent tectonic activity, raises the question of present-day strain accumulation in southern Africa. The low strain rates expected in such an intraplate setting may be difficult to measure geodetically, especially since the distribution of Global Positioning System (GPS) stations is sparse and uneven. Nevertheless, it is useful to try place an upper bound on regional strain accumulation using the existing permanent GPS stations. We therefore updated the analysis of data from openly available, continuously recording GPS stations in southern Africa to derive a continental-scale velocity field in order to search for region-wide deformation (supporting information and Figure 1).

We search for deviations from a purely rigid behavior by estimating a single rigid rotation for the whole region considered here and examining residual velocities. We find no spatial pattern in residual velocities with respect to a rigid plate (Figure 1) with an root-mean-square misfit of 0.25 mm/year (maximum residual of 0.95 mm/year), and a χ^2 of 1.1. The comparison of the distribution of residual velocities, normalized by their uncertainty, with that of a two-dimensional, unit variance, normal distribution shows that the velocities are well described by a random process (Figure 1). Although the uneven geographic distribution of GPS stations in southern Africa is not optimal for this type of study, our results rule out the possibility of broad-scale deformation at a level of 0.25 mm/year, consistent with observations in several other plate interiors (Craig & Calais, 2014; Nocquet, 2012; Tregoning et al., 2013), as well as previous results in the same region (Hackl et al., 2011; Saria et al., 2014).

6. What Caused the Botswana Earthquake?

The 2017, M_w6.5, Botswana earthquake occurred in an area with no previous evidence of similar magnitude events, low and diffuse background seismicity, and no topographic features indicative of repeated recent

faulting, characteristics that are shared by most large earthquakes in stable continental regions (Calais et al., 2016). That the earthquake focal mechanism shows purely normal faulting is consistent with the occurrence of other normal faulting earthquakes within stable southern Africa (Heidbach et al., 2016) and with stress models derived from horizontal gradients of gravitational potential energy (Coblentz & Sandiford, 1994; Stamps et al., 2014). Both indicate an extensional stress state with a subvertical maximum principal compressive stress (σ_1) and a subhorizontal least principal compressive stress (σ_3).

However, a striking feature of the event is its depth, which all authors consistently find between 25 and 30 km, well into the lower part of a crust that is around 35 km thick in the epicentral area (Nguuri et al., 2001; Tedla et al., 2011; Youssof et al., 2013). The occurrence of earthquakes in the lower crust is often interpreted as evidence for a mafic composition (Albaric et al., 2008; Craig et al., 2011; Nyblade & Langston, 1995; Shudofsky et al., 1987). Seismic data in the Kaapval craton, however, show a low Poisson ratio of 0.25 for the whole crust and a 2,860 kg/m^3 lowermost crust density, indicative of a felsic composition (James et al., 2003), consistent with the lack of mafic granulite xenoliths from the lower Kaapvaal crust (Schmitz & Bowring, 2003).

Given a crustal geotherm derived from local surface heat flow measurements, crustal yield strength envelopes for the region (Figure 4a) show that brittle failure should not happen at such depth, under hydrostatic pore fluid pressure, as a felsic lower crust flows at low differential stress. In the absence of a mafic lower crust, (1) the maximum differential stress that can be maintained at hypocentral depth is about 50–100 MPa and (2) deformation at such depth is controlled by viscous flow. However, if pore fluid pressure becomes sublithostatic, brittle failure on a 73° dip fault is allowed at a differential stress lower than 50 MPa (Figure 4c). Alternate mechanisms are also possible, such as thermal shear runaway, rupture of a brittle asperity, or dehydration reactions (e.g., Green & Houston, 1995; Prieto et al., 2013). The former two require significant, ongoing, shear motion, which is unlikely in this stable cratonic environment. The latter implies a phase transition, which would require a recent rejuvenation of the cratonic crust that is not documented. The stability of the cratonic crust requires an external forcing to trigger this event.

Therefore, a likely explanation for the Botswana earthquake is that it was triggered by elevated, sublithostatic, pore fluid pressure that enabled failure at the low differential stress that prevails in the viscous lower crust (Gold & Soter, 1985). The observed foreshock swarm-like sequences may be the signature of the initiation of a pulse of high pore fluid pressure (Balfour et al., 2015; Hainzl & Fischer, 2002; Reyners et al., 2007). Field observations show numerous evidence of fluid-assisted embrittlement in the viscous regime of deformation (Handy et al., 2007; Wehrens et al., 2016). Lower-crustal earthquakes in the northern Alpine foreland (Deichmann, 1992) and beneath the Flinders Ranges of South Australia (Balfour et al., 2015) have been interpreted as the result of a decrease of effective stress on preexisting faults by fluids at near-lithostatic pore pressure, allowing a switch from viscous to brittle deformation. In the later case, the authors argued for a deep fluid source from a remnant hydrated mantle on the basis of elevated ^{3}He/^{4}He ratios in springs, as also observed in Vogtland, Bohemia, and Eger Rift intraplate seismicity areas of central Europe (Bräuer et al., 2009; Weise et al., 2001). In the Taupo active rift (New Zealand), lower-crustal earthquakes in the viscous regime are interpreted as triggered by fluids migrating upward from the hydrated Hikurangi subduction mantle wedge (Reyners et al., 2007).

Southern Africa is a largely cratonic province characterized by widespread kimberlite outcrops, which take their source in carbonate-rich matrices and parental magma (Kamenetsky et al., 2014). Rapid kimberlite melt ascent through the crust is assumed to be driven by the exsolution of a H_2O- and CO_2-rich fluid phases at mantle depths (Russell et al., 2012). This requires the presence of volatiles in the mantle, which can be hosted in the lower lithosphere until remobilization under large-scale tensional tectonic stresses as shown in the Virunga volcanic field of the East African Rift (Hudgins et al., 2015). In the Okavango basin, 350 km north of the Botswana earthquake, a thermal anomaly measured in the absence of surface magmatism and of a thinned or altered lithosphere is interpreted as the signature of fluids advected from a metasomatized lithospheric mantle (Leseane et al., 2015). Therefore, several lines of evidence point to the presence of significant amounts of fluids in the upper mantle underneath southern and eastern Africa. The upward migration of these deep and buoyant fluids could perhaps explain the locally elevated pore fluid pressure necessary to trigger seismicity in the otherwise ductile lower crust of the Kaapval craton.

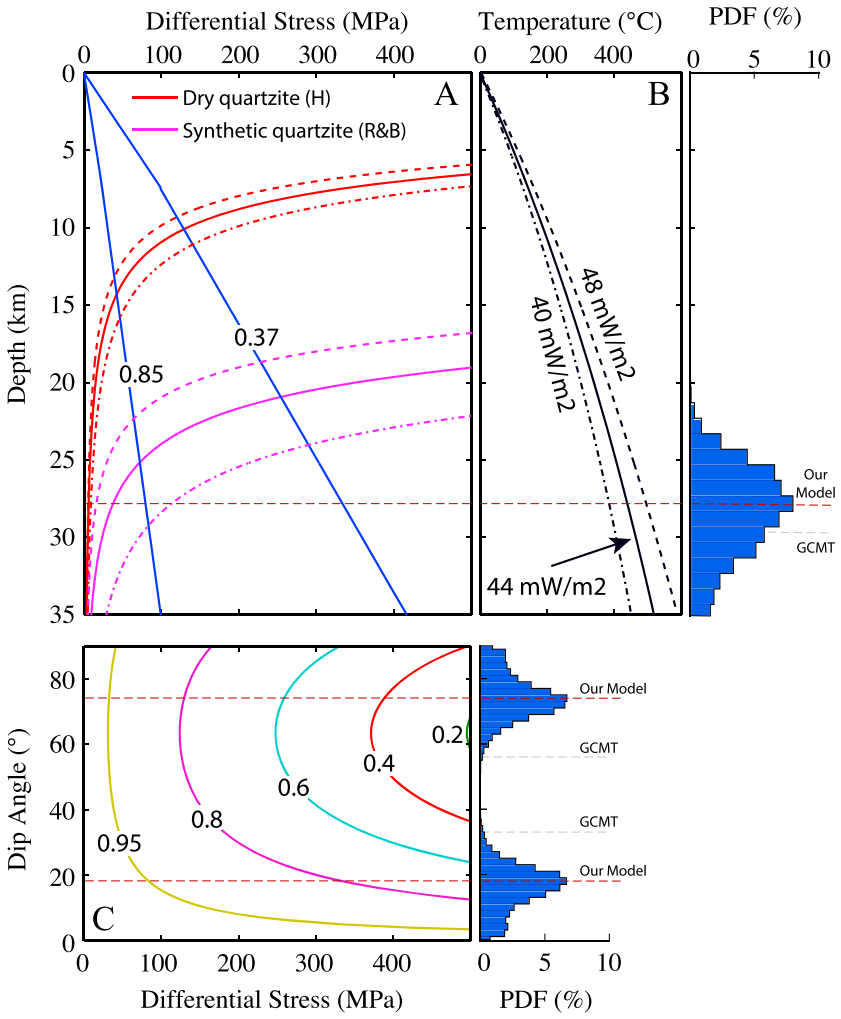

Figure 4. Mechanical behavior of rocks and earthquake source parameters. (a) Red and magenta lines show dislocation creep flow laws using dry and synthetic quartzite rheologies for three geotherms shown on panel (b). Flow law parameters for wet quartzite are from Rutter and Brodie (2004) and for dry quartzite from (Hirth et al., 2001). Strain rate is 10×10^{-18} s^{-1}. We use a surface heat flow of 44 mW/m^2 and the average of four close-by measurements (Ballard et al., 1987) and computed the corresponding crustal geotherm (Russel & Kopylova, 1999). Blue lines show friction law for hydrostatic ($\lambda_V = 0.37$) and sublithostatic ($\lambda_V = 0.85$) pore fluid pressure (Byerlee, 1978). (b) Geotherms derived from a surface heat flow of 44 ±10% mW/m^2 calculated following Russel and Kopylova (1999). (c) Differential stress ($\sigma_1 - \sigma_3$) required for frictional reactivation of cohesionless normal faults at 30-km depth as a function of their dip angle for different values of the pore fluid factor λ_V, following Sibson (1989). Lithostatic conditions correspond to $\lambda_V = 1$. Histograms are the probability density functions of the earthquake source parameters estimated from interferometric synthetic aperture radar data, including centroid depth and dip angle. PDF = probability density function.

7. Conclusion

The occurrence of the 3 April 2017 Botswana earthquake in a felsic lower crust where viscous deformation should prevail indicates that pore fluid pressure elevated to sublithostatic played a key role in triggering the rupture. The two swarm-like sequences of earthquakes that preceded the main Botswana event in December and March 2017 may be further evidence for fluid movement in a critically loaded fault network, which eventually led to a large event. Finally, the damage caused by the mainshock potentially led to a decrease in pore fluid pressure locally, turning off the activity of this swarm-like sequence, hence the detection of a classic Omori decay of aftershock productivity.

The Botswana earthquake therefore did not require localized, present-day, stress, or strain accumulation, contrary to plate boundary events resulting from the near-fault accrual of stress imposed by plate and block motions (Kanamori & Brodsky, 2004). In a prestressed crust able to store reversible strain on long timescales

(Craig et al., 2016; Feldl & Bilham, 2006) with faults at or close to failure (Townend & Zoback, 2000), short-term fault strength transients, such as those triggered by fluids leaks from the upper mantle, may be all it takes to trigger large events.

Acknowledgments
We thank IRIS for granting access to seismic data (http://ds.iris.edu/SeismiQuery). Sentinel-1A and Sentinel-B acquisitions were downloaded through the Plateforme d'Exploitation des Produits Sentinel (PEPS, https://peps.cnes.fr) of the Centre National des Études Spatiales (CNES). The seismic catalog was downloaded through the ISC website (http://www.isc.ac.uk/). Global Precipitation Measurement data are available for download at https://pmm.nasa.gov/GPM. B. G. received funding from the European Research Council (ERC) under the European Union's Horizon 2020 research and innovation program (REALISM project, grant agreement 681346). R. J. received funding from the European Research Council (ERC) under the European Union's Horizon 2020 research and innovation program (Geo-4D project, grant agreement 758210). E. C. acknowledges support from the Institut Universitaire de France and from the INSU/CNRS Tellus-Rift program. We thank K. Materna and an anonymous reviewer for the time they took at evaluating our work and their constructive comments.

References

Albano, M., Polcari, M., Bignami, C., Moro, M., Saroli, M., & Stramondo, S. (2017). Did anthropogenic activities trigger the 3 April 2017 M_W 6.5 Botswana earthquake? *Remote Sensing*, *9*(12), 1028. https://doi.org/10.3390/rs9101028

Albaric, J., Déverchère, J., Petit, C., Perrot, J., & Le Gall, B. (2008). Crustal rheology and depth distribution of earthquakes: Insights from the central and southern East African Rift System. *Tectonophysics*, *468*(1), 28–41.

Allman, A., & Smolka, A. (2001). Increasing loss potential in earthquake risk—A reinsurance perspective. In T. Camelbeeck (Ed.), *Proceedings of the Workshop: Evaluation of the Potential for Large Earthquakes in Regions of Present-Day Low Seismic Activity in Europe* (pp. 1–4). Han-sur-Lesse, Belgium.

Balfour, N. J., Cummins, P. R., Pilia, S., & Love, D. (2015). Localization of intraplate deformation through fluid-assisted faulting in the lower-crust: The Flinders Ranges, South Australia. *Tectonophysics*, *655*, 97–106. https://doi.org/10.1016/j.tecto.2015.05.014

Ballard, S., Pollack, H. N., & Skinner, N. J. (1987). Terrestrial heat flow in Botswana and Namibia. *Journal of Geophysical Research*, *92*(B7), 6291–6300.

Bouchon, M., Karabulut, H., Aktar, M., Ozalaybey, S., Schmittbuhl, J., & Bouin, M. (2011). Extended nucleation of the 1999 M_w 7.6 Izmit earthquake. *Science*, *331*(6019), 877–880. https://doi.org/10.1126/science.1197341

Bowman, J. R. (1992). The 1988 Tennant Creek, northern territory, earthquakes: A synthesis. *Australian Journal of Earth Sciences*, *39*(5), 651–669.

Bräuer, K., Kämpf, H., & Strauch, G. (2009). Earthquake swarms in non-volcanic regions: What fluids have to say. *Geophysical Research Letters*, *36*, L17309. https://doi.org/10.1029/2009GL039615

Byerlee, J. (1978). Friction of rocks. *Pure and Applied Geophysics*, *116*(4-5), 615–626.

Calais, E., Camelbeeck, T., Stein, S., Liu, M., & Craig, T. J. (2016). A new paradigm for large earthquakes in stable continental plate interiors. *Geophysical Research Letters*, *43*, 10,621–10,637. https://doi.org/10.1002/2016GL070815

Coblentz, D. D., & Sandiford, M. (1994). Tectonic stresses in the African plate: Constraints on the ambient lithospheric stress state. *Geology*, *22*(9), 831–834.

Craig, T. J., & Calais, E. (2014). Strain accumulation in the New Madrid and Wabash Valley seismic zones from 14 years of continuous GPS observation. *Journal of Geophysical Research: Solid Earth*, *119*, 9110–9129. https://doi.org/10.1002/2014JB011498

Craig, T. J., Calais, E., Fleitout, L., Bollinger, L., & Scotti, O. (2016). Evidence for the release of long-term tectonic strain stored in continental interiors through intraplate earthquakes. *Geophysical Research Letters*, *43*, 6826–6836. https://doi.org/10.1002/2016GL069359

Craig, T. J., Jackson, J. A., Priestley, K., & McKenzie, D. (2011). Earthquake distribution patterns in Africa: Their relationship to variations in lithospheric and geological structure, and their rheological implications. *Geophysical Journal International*, *185*(1), 403–434.

Deichmann, N. (1992). Structural and rheological implications of lower-crustal earthquakes below northern Switzerland. *Physics of the Earth and Planetary Interiors*, *69*, 270–280.

Ekström, G., Nettles, M., & Dziewonski, A. M. (2012). The global CMT project 2004–2010: Centroid-moment tensors for 13,017 earthquakes. *Physics of the Earth and Planetary Interiors*, *200–201*, 1–9. https://doi.org/10.1016/j.pepi.2012.04.002

Farr, T. G., & Kobrick, M. (2000). Shuttle radar topography mission produces a wealth of data. *Eos, Transactions of the American Geophysical Union*, *81*(48), 583–585.

Feldl, N., & Bilham, R. (2006). Great Himalayan earthquakes and the Tibetan plateau. *Nature*, *444*, 165–170. https://doi.org/10.1038/nature05199

Gardonio, B. (2017). Seismic and aseismic slip: The Japanese subduction zone (PhD thesis), Université Savoie Mont Blanc.

Gold, T., & Soter, S. (1985). Fluid ascent through the solid lithosphere and its relation to earthquakes. *Pure and Applied Geophysics*, *122*(2-4), 492–530.

Green, H. W., & Houston, H. (1995). The mechanics of deep earthquakes. *Annual Review of Earth and Planetary Sciences*, *23*, 169–213. https://doi.org/10.1146/annurev.ea.23.050195.001125

Hackl, M., Malservisi, R., Hugentobler, U., & Wonnacott, R. (2011). Estimation of velocity uncertainties from GPS time series: Examples from the analysis of the South African TrigNet network. *Journal of Geophysical Research*, *116*, B11404. https://doi.org/10.1029/2010JB008142

Hainzl, S., & Fischer, T. (2002). Indications for a successively triggered rupture growth underlying the 2000 earthquake swarm in Vogtland/NW Bohemia. *Journal of Geophysical Research*, *107*(B12), ESE 5–1–ESE 5–9. https://doi.org/10.1029/2002JB001865

Handy, M., Hirth, G., & Burgmann, R. (2007). Continental fault structure and rheology from the frictional-to-viscous transition downward. In M. R. Handy, G. Hirth, & N. Hovius (Eds.), *Tectonic Faults: Agents of Change on a Dynamic Earth* (pp. 139–181). Cambridge, MA: MIT Press.

Heidbach, O., Rajabi, M., Reiter, K., Ziegler, M., & Team, W. (2016). World stress map database release 2016. GFZ Data Services, https://doi.org/10.5880/WSM.2016.001

Hirth, G., Teyssier, C., & Dunlap, J. W. (2001). An evaluation of quartzite flow laws based on comparisons between experimentally and naturally deformed rocks. *International Journal of Earth Sciences*, *90*, 77–87.

Hough, S. E., Armbruster, J. G., Seeber, L., & Hough, J. F. (2000). On the modified Mercalli intensities and magnitudes of the 1811–1812 New Madrid earthquakes. *Journal of Geophysical Research*, *105*, 23,839–23,864.

Hudgins, T. R., Mukasa, S. B., Simon, A. C., Moore, G., & Barifaijo, E. (2015). Melt inclusion evidence for CO_2-rich melts beneath the western branch of the East African Rift: Implications for long-term storage of volatiles in the deep lithospheric mantle. *Contributions to Mineralogy and Petrology*, *169*(5), 46.

James, D. E., Niu, F., & Lithos, J. R. (2003). Crustal structure of the Kaapvaal craton and its significance for early crustal evolution. *Lithos*, *71*, 413–429.

Johnston, A. C. (1989). The seismicity of 'stable continental interiors'. In S. Gregersen & P. W. Basham (Eds.), *Earthquakes at North-Atlantic Passive Margins: Neotectonics and Postglacial Rebound* (pp. 2990–327). Dordrecht, Netherlands: Springer.

Johnston, A. C. (1996). Seismic moment assessment of earthquakes in stable continental regions—II. Historical seismicity. *Geophysical Journal International*, *125*(3), 639–678. https://doi.org/10.1111/j.1365-246X.1996.tb06015.x

Jolivet, R., Simons, M., Agram, P. S., Duputel, Z., & Shen, Z.-K. (2015). Aseismic slip and seismogenic coupling along the central San Andreas Fault. *Geophysical Research Letters*, *42*, 297–306. https://doi.org/10.1002/2014GL062222

Kamenetsky, V. S., Golovin, A. V., Maas, R., Giuliani, A., Kamenetsky, M. B., & Weiss, Y. (2014). Towards a new model for kimberlite petrogenesis: Evidence from unaltered kimberlites and mantle minerals. *Earth-Science Reviews*, *139*, 145–167.

Kanamori, H., & Brodsky, E. E. (2004). The physics of earthquakes. *Reports on Progress in Physics*, *67*(8), 1429–1496. https://doi.org/10.1088/0034-4885/67/8/R03

Kato, A., & Nakagawa, S. (2014). Multiple slow-slip events during a foreshock sequence of the 2014 Iquique, Chile M_w 8.1 earthquake. *Geophysical Research Letters*, *41*, 5420–5427. https://doi.org/10.1002/2014GL061138

Kato, A., Obara, K., Igarashi, T., Tsuruoka, H., Nakagawa, S., & Hirata, N. (2012). Propagation of slow slip leading up to the 2011 M_w 9.0 Tohoku-Oki earthquake. *Science*, *335*, 705–708. https://doi.org/10.1126/science.1215141

Kolawole, F., Atekwana, E. A., Malloy, S., Stamps, D. S., Grandin, R., Abdelsalam, M. G., et al. (2017). Aeromagnetic, gravity, and differential interferometric synthetic aperture radar analyses reveal the causative fault of the 3 April 2017 M_w6.5 Moiyabana, Botswana, earthquake. *Geophysical Research Letters*, *44*, 8837–8846. https://doi.org/10.1002/2017GL074620

Kruger, F., & Scherbaum, F. (2014). The 29 September 1969, Ceres, South Africa, earthquake: Full waveform moment tensor inversion for point source and kinematic source parameters. *Bulletin of the Seismological Society of America*, *104*(1), 576–581.

Lengliné, O., Enescu, B., Peng, Z., & Shiomi, K. (2012). Decay and expansion of the early aftershock activity following the 2011, M_w9.0 Tohoku earthquake. *Geophysical Research Letters*, *39*, L18309. https://doi.org/10.1029/2012GL052797

Lengliné, O., & Marsan, D. (2009). Inferring the coseismic and postseismic stress changes caused by the 2004 Mw = 6 Parkfield earthquake from variations of recurrence times of microearthquakes. *Journal of Geophysical Research*, *114*, B10303. https://doi.org/10.1029/2008JB006118

Leseane, K., Atekwana, E. A., Mickus, K. L., Abdelsalam, M. G., Shemang, E. M., & Atekwana, E. A. (2015). Thermal perturbations beneath the incipient Okavango Rift Zone, northwest Botswana. *Journal of Geophysical Research: Solid Earth*, *120*, 1210–1228. https://doi.org/10.1002/2014JB011029

Liu, M., & Stein, S. (2016). Mid-continental earthquakes: Spatiotemporal occurrences, causes, and hazards. *Earth-Science Reviews*, *162*, 364–386.

Modisi, M. P., Atekwana, E. A., Kampunzu, A. B., & Ngwisanyi, T. H. (2000). Rift kinematics during the incipient stages of continental extension: Evidence from the nascent Okavango rift basin, northwest Botswana. *Geology*, *28*(10), 939–942.

Nguuri, T. K., Gore, J., James, D. E., Webb, S. J., Wright, C., Zengeni, T. G., et al. (2001). Crustal structure beneath southern Africa and its implications for the formation and evolution of the Kaapvaal and Zimbabwe cratons. *Geophysical Research Letters*, *28*(13), 2501–2504. https://doi.org/10.1029/2000GL012587

Nocquet, J. M. (2012). Present-day kinematics of the Mediterranean: A comprehensive overview of GPS results. *Tectonophysics*, *579*(S1), 220–242.

Nuttli, O. W. (1973). The Mississippi Valley earthquakes of 1811 and 1812: Intensities, ground motion and magnitudes. *Bulletin of the Seismological Society of America*, *63*(1), 227–248.

Nyblade, A. A., & Langston, C. A. (1995). East African earthquakes below 20 km depth and their implications for crustal structure. *Geophysical Journal International*, *121*, 49–62.

Okada, Y. (1985). Surface deformation due to shear and tensile faults in a half-space. *Bulletin of the Seismological Society of America*, *75*(4), 1135–1154.

Pastier, A.-M., Dauteuil, O., Murray-Hudson, M., Moreau, F., Walpersdorf, A., & Makati, K. (2017). Is the Okavango Delta the terminus of the East African Rift System? Towards a new geodynamic model: Geodetic study and geophysical review. *Tectonophysics*, *712–713*, 469–481.

Peng, Z., & Zhao, P. (2009). Migration of early aftershocks following the 2004 Parkfield earthquake. *Nature Geoscience*, *2*, 877–881. https://doi.org/10.1038/ngeo697

Prieto, G. A., Florez, M., Barrett, S. A., Beroza, G. C., Pedraza, P., Blanco, J. F., & Poveda, E. (2013). Seismic evidence for thermal runaway during intermediate-depth earthquake rupture. *Geophysical Research Letters*, *40*, 6064–6068. https://doi.org/10.1002/2013GL058109

Reeves, C. V. (1972). Rifting in the Kalahari? *Nature*, *237*(5350), 95–96.

Reyners, M., Eberhart-Phillips, D., & Stuart, G. (2007). The role of fluids in lower-crustal earthquakes near continental rifts. *Nature*, *446*(7139), 1075–1078.

Ruiz, S., Metois, M., Fuenzalida, A., Ruiz, J., Leyton, F., Grandin, R., et al. (2014). Intense foreshocks and a slow slip event preceded the 2014 Iquique M_w 8.1 earthquake. *Science*, *345*(6201), 1165–1169. https://doi.org/10.1126/science.1256074

Russel, J. K., & Kopylova, M. G. (1999). A steady state conductive geotherm for the north central Slave, Canada: Inversion of petrological data from the Jericho Kimberlite pipe. *Journal of Geophysical Research*, *104*(B4), 7089–7101.

Russell, J. K., Porritt, L. A., Lavallée, Y., & Dingwell, D. B. (2012). Kimberlite ascent by assimilation-fuelled buoyancy. *Nature*, *481*(7381), 352–356.

Rutter, E. H., & Brodie, K. H. (2004). Experimental intracrystalline plastic flow in hot-pressed synthetic quartzite prepared from Brazilian quartz crystals. *Journal of Structural Geology*, *26*(2), 259–270.

Saria, E., Calais, E., Stamps, D. S., Delvaux, D., & Hartnady, C. (2014). Present-day kinematics of the East African Rift. *Journal of Geophysical Research: Solid Earth*, *119*, 3584–3600. https://doi.org/10.1002/2013JB010901

Schmitz, M. D., & Bowring, S. A. (2003). Ultrahigh-temperature metamorphism in the lower crust during Neoarchean Ventersdorp rifting and magmatism, Kaapvaal Craton, southern Africa. *GSA Bulletin*, *115*(5), 533–548.

Scholz, C. H., Koczynski, T. A., & Hutchins, D. G. (1976). Evidence for incipient rifting in southern Africa. *Geophysical Journal of the Royal Astronomical Society*, *44*(1), 135–144. https://doi.org/10.1111/j.1365-246X.1976.tb00278.x.

Shelly, D., Beroza, G., & Ide, S. (2007). Non-volcanic tremor and low-frequency earthquake swarms. *Nature*, *446*, 305–307. https://doi.org/10.1038/nature05666

Shudofsky, G. N., Cloetingh, S., Stein, S., & Wortel, R. (1987). Unusually deep earthquakes in East Africa: Constraints on the thermo-mechanical structure of a continental rift system. *Geophysical Research Letters*, *14*(7), 741–744.

Sibson, R. H. (1989). High-angle reverse faulting in northern New Brunswick, Canada, and its implications for fluid pressure levels. *Journal of Structural Geology*, *11*(7), 873–877.

Simons, M., Fialko, Y., & Rivera, L. (2002). Coseismic deformation from the 1999 Mw 7.1 Hector Mine, california, earthquake as inferred from in SAR and GPS observations. *Bulletin of the Seismological Society of America*, *92*(4), 1390. https://doi.org/10.1785/0120000933

Stamps, D. S., Flesch, L. M., & Calais, E. (2014). Current kinematics and dynamics of Africa and the East African Rift System. *Journal of Geophysical Research: Solid Earth*, *119*, 5161–5186. https://doi.org/10.1002/2013JB010717

Tedla, G. E., Meijde, M. v. d., Nyblade, A. A., & Meer, F. D. v. d. (2011). A crustal thickness map of Africa derived from a global gravity field model using Euler deconvolution. *Geophysical Journal International*, *187*(1), 1–9. https://doi.org/10.1111/j.1365-246X.2011.05140.x

Townend, J., & Zoback, M. D. (2000). How faulting keeps the crust strong. *Geology*, *28*(5), 399–402.

Tregoning, P., Burgette, R., McClusky, S. C., Lejeune, S., Watson, C. S., & McQueen, H. (2013). A decade of horizontal deformation from great earthquakes. *Journal of Geophysical Research: Solid Earth*, *118*, 2371–2381. https://doi.org/10.1002/jgrb.50154

Wehrens, P., Berger, A., Peters, M., Spillmann, T., & Herwegh, M. (2016). Deformation at the frictional-viscous transition: Evidence for cycles of fluid-assisted embrittlement and ductile deformation in the granitoid crust. *Tectonophysics*, *693*(Part A), 66–84.

Weise, S. M., Bräuer, K., Kämpf, H., Strauch, G., & Koch, U. (2001). Transport of mantle volatiles through the crust traced by seismically released fluids: A natural experiment in the earthquake swarm area vogtland/NW Bohemia, Central Europe. *Tectonophysics*, *336*(1-4), 137–150. https://doi.org/10.1016/S0040-1951(01)00098-1

Xu, W., Dutta, R., & Jónsson, S. (2015). Identifying active faults by improving earthquake locations with InSAR data and Bayesian estimation: The 2004 Tabuk (Saudi Arabia) earthquake sequence. *Bulletin of the Seismological Society of America*, *105*(2A), 765–775. https://doi.org/10.1785/0120140289

Youssof, M., Thybo, H., Artemieva, I. M., & Levander, A. (2013). Moho depth and crustal composition in southern Africa. *Tectonophysics*, *609*(C), 267–287.